Chapter 14

CATHODES BASED ON $LiCoO_2$ AND $LiNiO_2$

Byungwoo Park[1], Yong Jeong Kim[1], and Jaephil Cho[2]

[1]*School of Materials Science and Engineering, and Research Center for Energy Conversion and Storage, Seoul National University, Seoul, Korea*
[2]*Department of Applied Chemistry, Kumoh National Institute of Technology, Gumi, Korea*

1. $LiCoO_2$ CATHODE MATERIALS

1.1. Introduction

Li-ion cells consisting of $LiMeO_2$ (Me: a 3*d*-transition metal element) and carbon materials have been of interest because of their capability to be safely operated for thousands of cycles whilst retaining a high energy density. Materials with the above formula more extensively examined for positive electrodes include $LiCoO_2$, $LiNiO_2$, $LiCo_{1-x}Ni_xO_2$, and $LiMnO_2$. Among these, more research has been done on $LiCoO_2$ because of its high energy density and good cycling performance. The electrochemical properties of cathodes based on $LiCoO_2$ are shown in Table 1 [1-5]. $LiCoO_2$ has served as an archetypal cathode material for secondary Li batteries ever since the discovery by Mizushima *et al.* [6] that Li can be reversibly removed (deintercalated) from and reinserted (intercalated) into Li_xCoO_2. The layered form of $LiCoO_2$, which has a rhombohedral symmetry belonging to the space group $R\bar{3}m$, is ideally suited to accommodate large changes of the Li content, x. This crystal structure consists of close-packed oxygen layers stacked in an *ABCABC* sequence with Co and Li ions residing in octahedral sites in alternating layers between the oxygen planes [7]. Figure 1 illustrates the crystal structure of $LiCoO_2$. As the Li concentration is changed in Li_xCoO_2, vacancies are either created or filled within the Li planes.

Table 1. Cycling stability of cathodes based on $LiCoO_2$.

Cathode Material	Capacity	Voltage Range	Ref.
$LiCoO_2$	157 mAh/g (initial) 120 mAh/g (50 cycles)	4.35 - 2.5 V 0.4 mA/cm^2	1
	151 mAh/g (initial) 128 mAh/g (30 cycles)	4.3 - 3.0 V 0.5 mA/cm^2	2
$LiAl_{0.25}Co_{0.75}O_2$	127 mAh/g (initial) 64 mAh/g (9 cycles)	4.5 - 2.0 V 0.4 mA/cm^2	3
	80 mAh/g (initial) 35 mAh/g (10 cycles)	4.3 - 2.5 V 0.4 mA/cm^2	4
$LiMg_{0.05}Co_{0.95}O_2$	143 mAh/g (initial) 125 mAh/g (30 cycles)	4.3 - 3.0 V 0.5 mA/cm^2	2
	158 mAh/g (initial) 141 mAh/g (30 cycles)	4.3 - 2.9 V 0.5 mA/cm^2	5

Li_xCoO_2 exhibits many of the essential properties required for a reliable cathode material. The voltage of Li_xCoO_2 is sufficiently high to guarantee a high-energy density, although it is not too high to cause electrolyte decomposition. Furthermore, Li_xCoO_2 undergoes small structural changes as Li is deintercalated to a concentration of approximately 0.5. In addition to its favorable electrochemical properties, Li_xCoO_2 also exhibits phase transformations that are typical of many intercalation compounds.

Figure 2 [8] shows the evolution of the lattice constants *a* and *c* as a function of x in Li_xCoO_2, and the global phase diagram for Li_xCoO_2. *In-situ* x-ray diffraction indicates a sequence of three distinct phase transitions as x is varied from 1 to 0.4. Two of the transitions are situated slightly above and below x = 0.5, and are caused by an order-disorder transition of the lithium ions [8,9]. Reimers and Dahn [8], for example, observed that Li ions are ordered in rows at x = 0.5. They carefully measured the stability region of this ordered phase and determined its order-disorder transition temperature to be approximately 60°C (Fig. 2). The order-disorder (monoclinic-hexagonal phase) transition has been studied as a function of temperature, allowing the determination of an order-disorder diagram. The other phase transition is shown to be first order (hexagonal I + II) involving a significant expansion of the lattice constant *c* of the hexagonal unit cell [8,9].

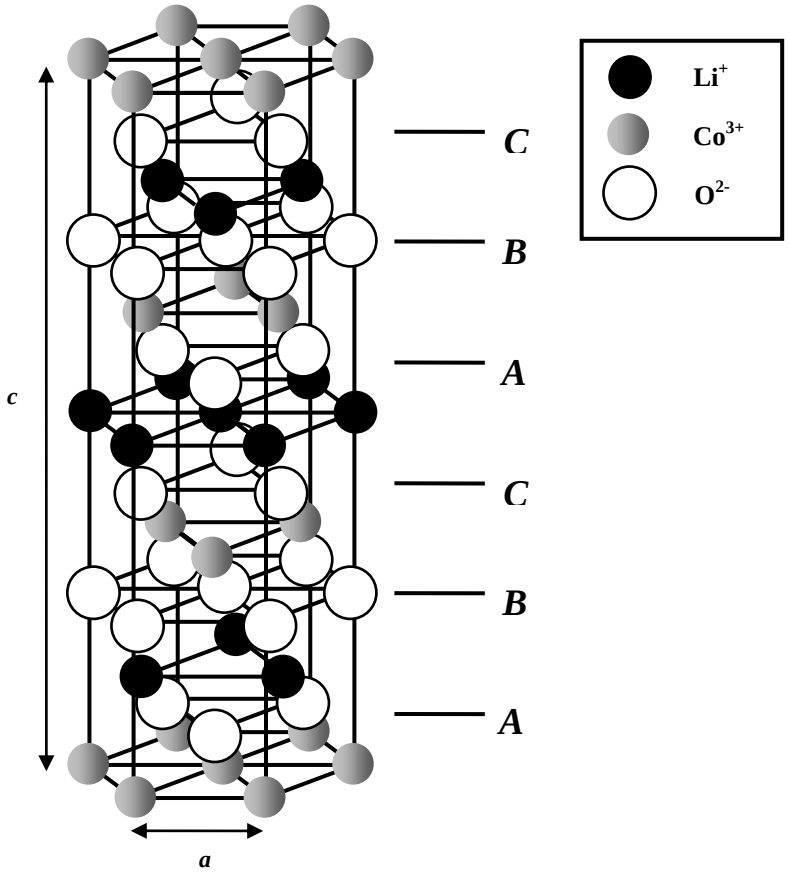

Figure 1. Schematic diagram of the layered $LiCoO_2$ structure.

Another transformation of an electronic nature occurs at a high Li concentration: $LiCoO_2$ is a semiconductor [10] while Li_xCoO_2 at concentrations below x = 0.75 is metallic [11], suggesting that a metal-insulator transition occurs at the intermediate Li concentration. Intriguingly, superimposed on this metal-insulator transition is the two-phase coexistence region between two crystallographically identical host hexagonal structures. At room temperature, this two-phase coexistence region is found to exist between the Li concentrations of x = 0.75 and 0.93

[8,9], as shown in Fig. 2. Amatucci *et al.* [12] reported that Li_xCoO_2 can be completely and reversibly deintercalated to slabs, held together by van der Waals forces, slide with respect to each other, so that the close-packed oxygen layers have an *ABAB* stacking sequence, as opposed to the *ABCABC* sequence of $LiCoO_2$.

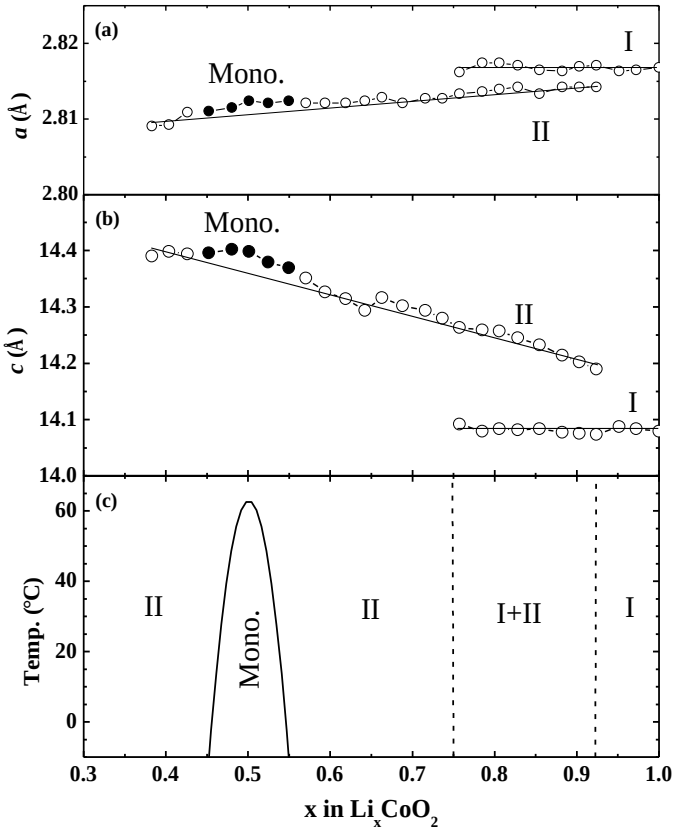

Figure 2. Lattice constants *a* (a) and *c* (b) as a function of the lithium concentration, x, in Li_xCoO_2. (c) Phase diagram for Li_xCoO_2 [8].

1.2. Capacity Fading Mechanisms in $LiCoO_2$ Cathode Materials

The theoretical capacity of a $LiCoO_2$ cathode is 274 mAh/g. However, in practical cells, the capacity is limited to about 140 mAh/g. This value corresponds to the range $0.5 < x < 1$ in Li_xCoO_2, with the cutoff voltage of approximately 4.2 V (with respect to a Li metal). To achieve more than 50% of its theoretical capacity, one must charge the Li_xCoO_2 to above 4.2 V. However, this generally causes a rapid loss of capacity with increasing cycle number. Cycling above 4.2 V leads to a dramatic increase in the capacity fade, which has been closely related to structural changes involving a decrease in the unit-cell volume [1,13-19], and an increase of cobalt dissolution into the electrolyte [20].

As shown in Fig. 2(a) and (b), the lattice constant *a* shows only minor changes during Li deintercalation. This is quite the opposite to the lattice constant *c*, which exhibits an expansion of up to 2-3% at $x \cong 0.5$, followed by a decrease for larger x [9,12]. Therefore, the lattice strain is both anisotropic and directly correlated with the lithium concentration. A $LiCoO_2$ cathode, like most oxides, can tolerate some elastic strain prior to fracture [1]. This property has been mainly attributed to the mechanical failure associated with the large lattice expansion along the *c*-axis direction. Figure 3 [1] shows individual highly-strained particles where microcracks are clearly visible (indicated by arrows), after 50 cycles between 2.5 and 4.35 V. It is also observed that the fractured particles sometimes contain an unstrained region, apparently relieved from the stress by the fracture event (Fig. 3(b)).

$LiCoO_2$/liquid electrolyte/Li cells were cycled to upper voltages in the range 4.1 - 4.5 V. The cells were then floated at each voltage for two weeks to allow the system to reach equilibrium. The cells were disassembled and quantitatively analyzed for the presence of cobalt on the anode through the use of atomic absorption spectroscopy. Figure 4 [20] shows that for voltages of 4.1 and 4.2 V versus Li metal, cobalt dissolution in the liquid electrolyte (1 M $LiPF_6$ in ethylene carbonate (EC) : dimethyl carbonate (DMC) (67:33 vol. %)) is very low, as is the capacity fade. However, a marked increase in cobalt loss is found when the cells are cycled to 4.3 V. Cycling to 4.4 V further increases the cobalt loss, and 4.5 V shows another sharp increase in the amount of cobalt dissolution. Cobalt dissolution is indeed related to the capacity loss with cycling above the traditional reversible voltage limit of 4.2 V.

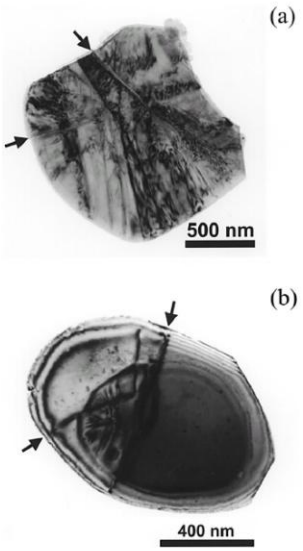

Figure 3. Severely damaged $LiCoO_2$ particles from a cycled cathode showing microfractures (arrows) and a strong diffraction contrast from the internal strain and extended defects [1].

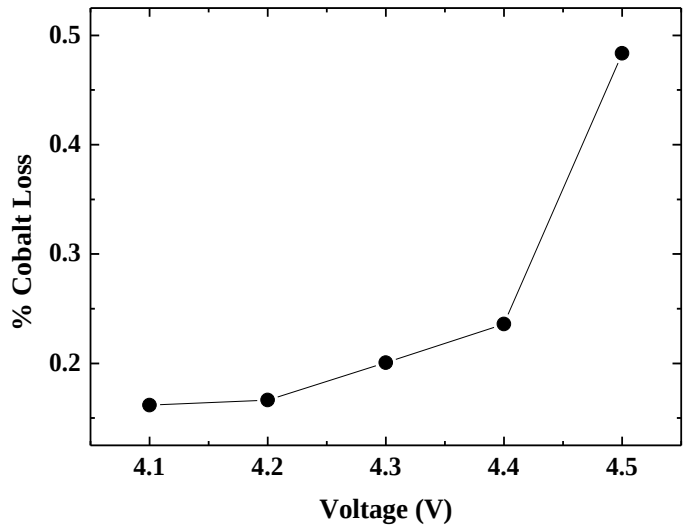

Figure 4. Cobalt loss (percentage) as a function of cycling voltage [20].

1.3. Electrochemical Properties of $LiCoO_2$ Cathode

$LiCoO_2$ powders are typically prepared by reacting a mixture of $LiOH \cdot H_2O$ and Co_3O_4 in the mole ratio of 1.05:1 at 900°C for 24 h. An excess amount of $LiOH \cdot H_2O$ is used to compensate for the loss of Li during firing. Figure 5 shows the XRD patterns of $LiCoO_2$ powders before cycling. The starting materials have a well-ordered α-$NaFeO_2$ structure.

Figure 6 shows the first charge and discharge curves for $LiCoO_2$, which indicate an initial capacity of 174 mAh/g between 4.4 and 2.75 V at a rate of 0.1 C (14 mA/g) in the half cell Li/$LiCoO_2$. The flat potential plateau at ~3.93 V is characteristic of the two-hexagonal-phase region [8,9]. Two additional plateaus at ~4.1 and ~4.2 V are attributed to the order-disorder transition (changes between monoclinic and hexagonal phases) occurring at $x \cong 0.5$ [8,9]. Figure 7 shows the cycle-life performance of a $LiCoO_2$ cathode with charge cutoff voltages of 4.4 V, 4.2 V, and 4.1 V at a rate of 0.5 C. The capacity losses at the charge cutoff voltage of 4.4 V, 4.2 V, and 4.1 V are ~52%, ~20%, and ~6%, respectively, after 50 cycles.

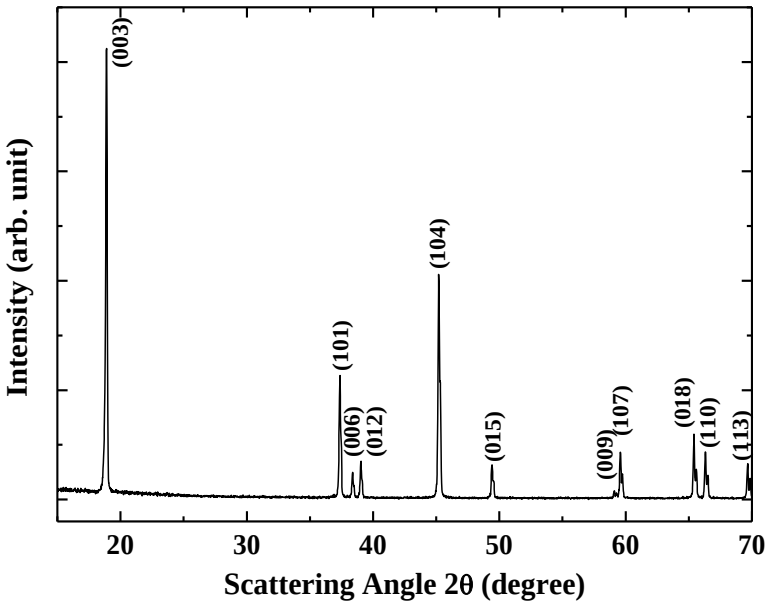

ig Figure 5. XRD patterns of the $LiCoO_2$ powders before cycling.

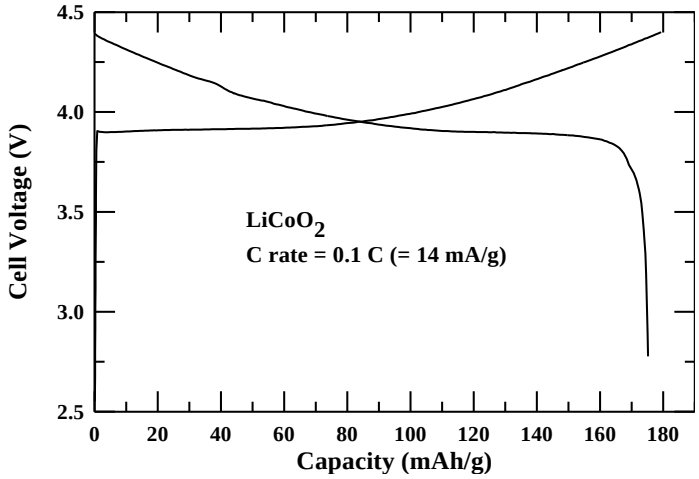

Figure 6. Voltage profiles of the $LiCoO_2$ cathode at a rate of 0.1 C (4.4 - 2.75 V).

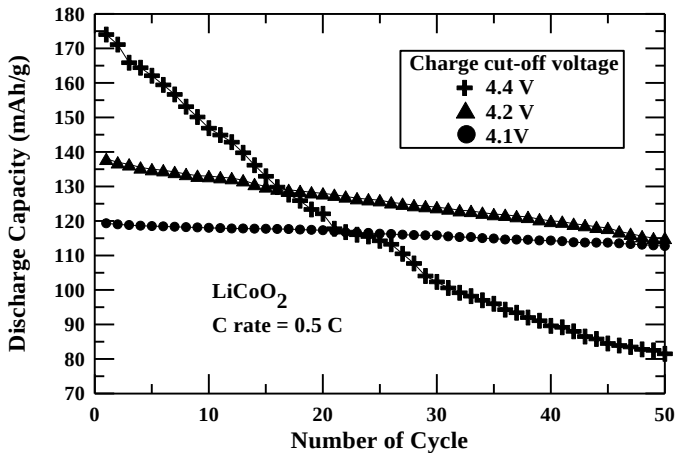

Figure 7. Cycle-life performance of the $LiCoO_2$ cathode with a charge cutoff voltage of 4.4 V, 4.2 V, and 4.1 V at the rate of 0.5 C. The discharge cutoff voltage is 2.75 V.

An evaluation of the cycle-life performance of $LiCoO_2$ was also carried out between 4.4 and 2.75 V in a coin-type Li-ion cell ($C/LiCoO_2$) (Fig. 8). The lower initial capacities of the $C/LiCoO_2$ cells (154 mAh/g) compared to the half-cells are due to the irreversible capacity loss of the mesophase pitch-based carbon fiber (MCF) anode.

For measuring the rate capability of a $LiCoO_2$ cathode, the charge rate is fixed at 0.5 C, and the discharge rates are increased from 0.2 to 0.5, 1, 2, and 3 C (Fig. 9). At higher C rates, the discharge voltage decreases more appreciably than the initial capacity.

Figure 10 shows the cyclic voltammograms (CVs) of $LiCoO_2$ conducted up to the second cycle. In this figure, *H* and *M* represent the hexagonal and monoclinic phases, respectively. Li diffusion in the oxide is a key factor that determines the rate at which a battery can be charged and discharged. With increasing interest in higher power density batteries, understanding the mechanisms of diffusion in insertion electrodes is important. The dependence of the Li^+ diffusion coefficient in the $LiCoO_2$ particles on the electrode potential is shown in Fig. 11 [21] – note the variation from $\sim 3\times10^{-10}$ to $\sim 7\times10^{-8}$ cm^2/sec. The Li diffusivities in the anodic (Li deintercalation) and cathodic (Li intercalation) scans are quite similar. Three minimum values corresponding to the CV peaks in Fig. 10 can be observed. It should be noted that the Li diffusivities exhibit minimum values at these peak potentials.

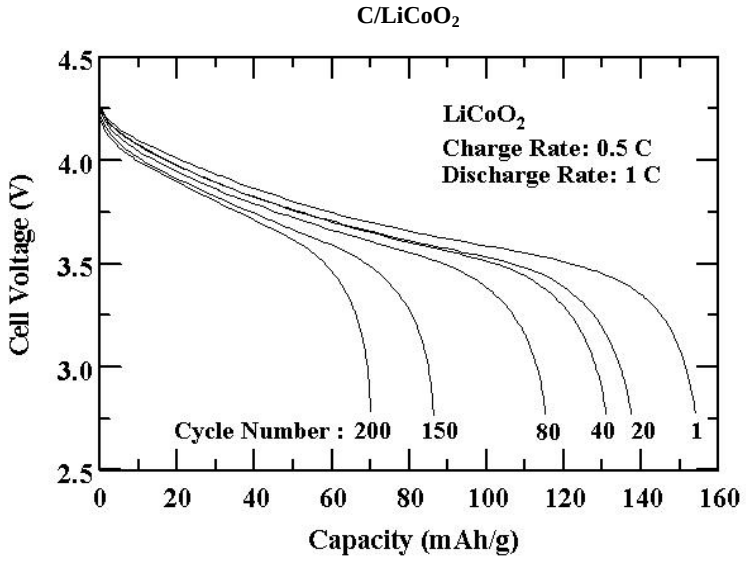

Figure 8. Plots of the capacity retention for C/$LiCoO_2$ cells as a function of cycle number. The charge and discharge rates are 0.5 and 1 C, respectively.

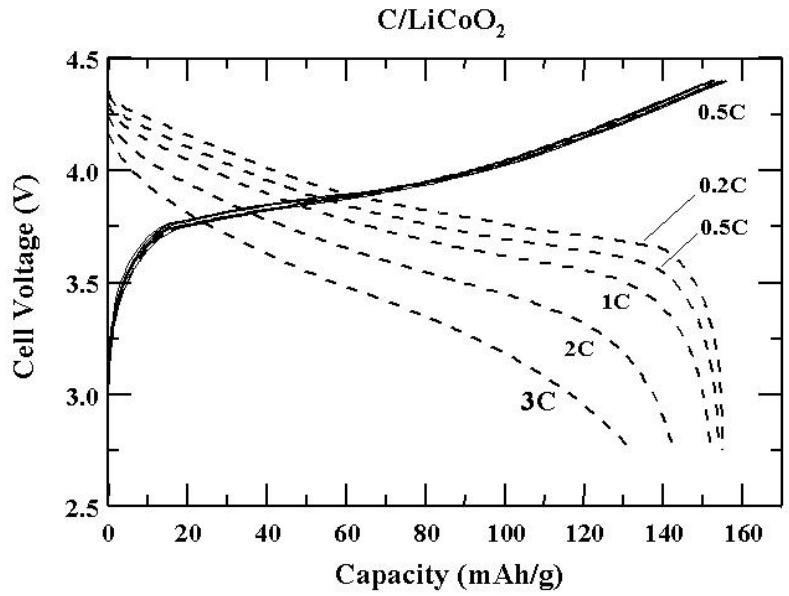

Figure 9. Rate capabilities of $LiCoO_2$ at various discharge rates of 0.2, 0.5, 1, 2, and 3 C. The charge rate was fixed at 0.5 C.

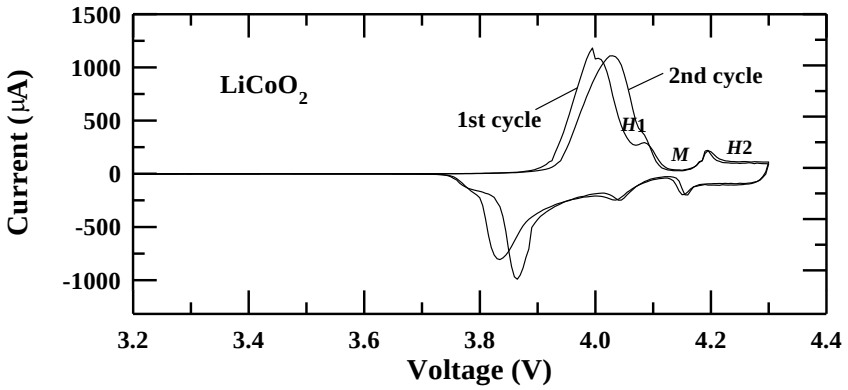

Figure 10. Cyclic voltammograms of a $LiCoO_2$ cathode. The scan rate was 0.02 mV/sec, and the symbols *H* and *M* denote the hexagonal and monoclinic phase, respectively.

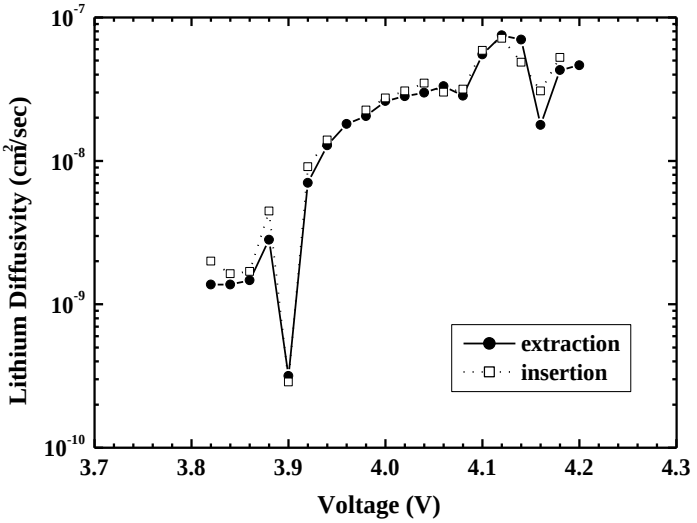

Figure 11. Dependence of the apparent diffusion coefficient of Li in the $LiCoO_2$ particles on the electrode potential (with a Li anode) [21].

1.4. Doping the $LiCoO_2$ Cathode

Although $LiCoO_2$ has excellent electrochemical properties, other materials such as $LiNiO_2$ and $LiMn_2O_4$ are being extensively studied as lower-cost and more environmentally-friendly substitutes. Efforts have also been made to synthesize solid solutions of $LiM_yCo_{1-y}O_2$ (M = Al, Mg, etc.) isostructural with $LiCoO_2$ [2-5,13,22,23]. Ceder *et al.* [22] reported that first-principles calculations could orient the search for possible cathode materials. Through such calculations, they have identified a large class of new candidate materials in which non-transition metals are substituted for cobalt. For one such material, $LiAl_yCo_{1-y}O_2$, they have predicted and experimentally verified that Al substitution raises the cell voltage while decreasing both the density of the material and its cost.

Figure 12 [3] shows the open-circuit voltage (equilibrium potential) as a function of the Li content in $LiCoO_2$, $LiAl_{0.25}Co_{0.75}O_2$, and $LiAl_{0.5}Co_{0.5}O_2$. The open-circuit voltage of the cells increases systematically with increasing Al content in the oxide. As shown in Fig. 13, during the first charge of $LiAl_{0.25}Co_{0.75}O_2$ between 2.0 and 4.5 V

at 0.4 mA/cm^2, 182 mAh/g is extracted at room temperature, and 219 mAh/g at 55°C, which correspond to 61 and 73% of the theoretical, respectively. The first discharge capacities are 127 mAh/g and 144 mAh/g at room temperature and 55°C, respectively. Rapid capacity fade is observed upon cycling at room temperature. After nine cycles, the discharge capacity decreases to 51% of the initial value. The Al-doped $LiCoO_2$ cathode shows both a reduced initial capacity relative to $LiCoO_2$, and a deteriorated capacity retention during cycling.

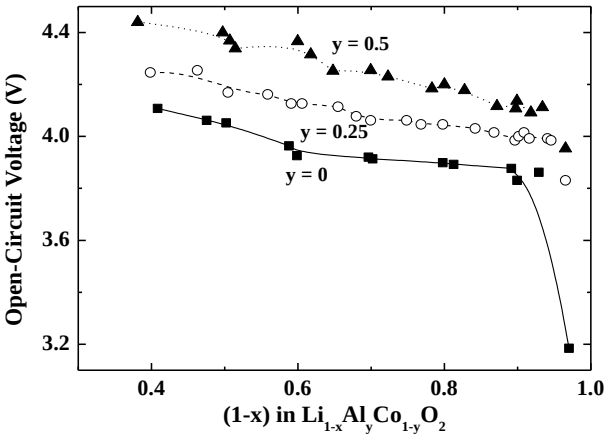

Figure 12. Open-circuit voltage (OCV) as a function of the Li content in pure $LiCoO_2$ and in Al-doped materials [3].

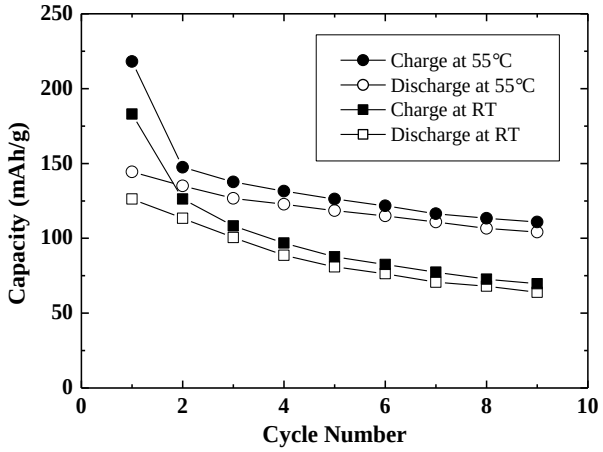

Figure 13. Specific capacity vs. cycle number for $LiAl_{0.25}Co_{0.75}O_2$, tested against a Li-metal anode at 0.4 mA/cm^2 between 2.0 and 4.5 V at room temperature and 55°C [3].

2. $LiNiO_2$ CATHODE MATERIALS

2.1. Introduction

Compared to $LiCoO_2$, $LiNiO_2$ is cheaper and less toxic. It delivers a larger reversible capacity with a comparable cycle life. It is considered to be one of the best cathode materials for Li-ion cells, and is used in graphite-based cells. The electrochemical properties of cathodes based on $LiNiO_2$ are shown in Table 2 [24-27]. However, its synthesis requires special care to obtain good and reproducible performances. Its structural and electrochemical behavior has been reviewed [24,25,28-30].

Table 2. Cycling stability of cathodes based on $LiNiO_2$.

Cathode Material	Capacity	Voltage Range	Ref.
$LiNiO_2$	220 mAh/g (initial) 70 mAh/g (100 cycles)	4.3 - 3.0 V 1 mA/cm^2	24
	195 mAh/g (initial) 150 mAh/g (30 cycles)	4.4 - 3.1 V 1 mA/cm^2	25
$LiNi_{0.70}Co_{0.30}O_2$	160 mAh/g (initial) 108 mAh/g (100 cycles)	4.3 - 2.75 V 2 mA/cm^2	26
$LiNi_{0.25}Co_{0.50}Mn_{0.25}O_2$	166 mAh/g (initial) 157 mAh/g (25 cycles)	4.4 - 2.5 V 0.6 mA/cm^2	27

2.2. Structure of $LiNiO_2$

The ideal structure of $LiNiO_2$ is a layered, isostructural with $LiCoO_2$. The XRD patterns of $LiNiO_2$ are indexed to a hexagonal symmetry with the space group $R\bar{3}m$, as shown in Fig. 14. However, the Li-Ni-O system is characterized by the existence of a $Li_{1-z}Ni_{1+z}O_2$ ($0 < z < 1$) solid solution. At low z values ($0 < z < 0.2$), the structure can still be described as a layered structure with the presence of Ni^{2+} cations within the Li layers. The amount, z, of interlayer Ni^{2+} cations depends on the

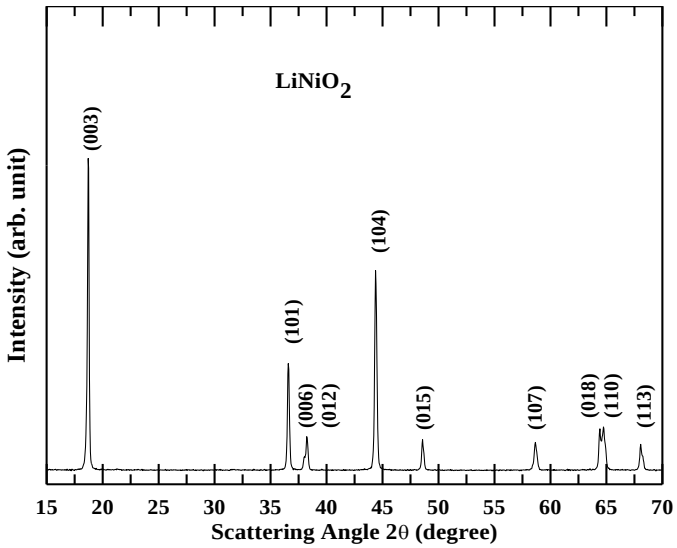

Figure 14. XRD patterns of the $LiNiO_2$ powders, before cycling.

synthesis conditions, and is lowered when using oxidizing atmospheres for the synthesis because of the stabilization of Ni^{3+}. The extra interlayer Ni^{2+} cations are strongly detrimental to the electrochemical performance, as they induce a lower capacity and larger polarization (voltage difference between the charge and discharge curves) [31-35].

2.3. Electrochemical Properties and Capacity Fading Mechanisms of $LiNiO_2$

As shown in Fig. 15, $LiNiO_2$ exhibits quite a large irreversible capacity loss during electrochemical cycling, much larger than that of $LiCoO_2$. Most of the irreversibility is observed at the end of the first charge, and a model based on the formation of inactive domains was proposed [36]. Another model [33,37], based on a local collapse of the interlayer space due to the oxidation of interlayer Ni^{2+} to smaller size Ni^{3+} cations ($r_{Ni^{2+}} = 0.68$ Å; $r_{Ni^{3+}} = 0.56$ Å), was proposed. Such a local contraction would impede Li reintercalation in the six close-neighboring sites of interlayer Ni^{3+} cations, due to the larger size of the Li^+ ion ($r_{Li^+} =$ 0.74 Å), which would lead to a fast increase of the irreversible capacity with increasing quantities of initial interlayer cations.

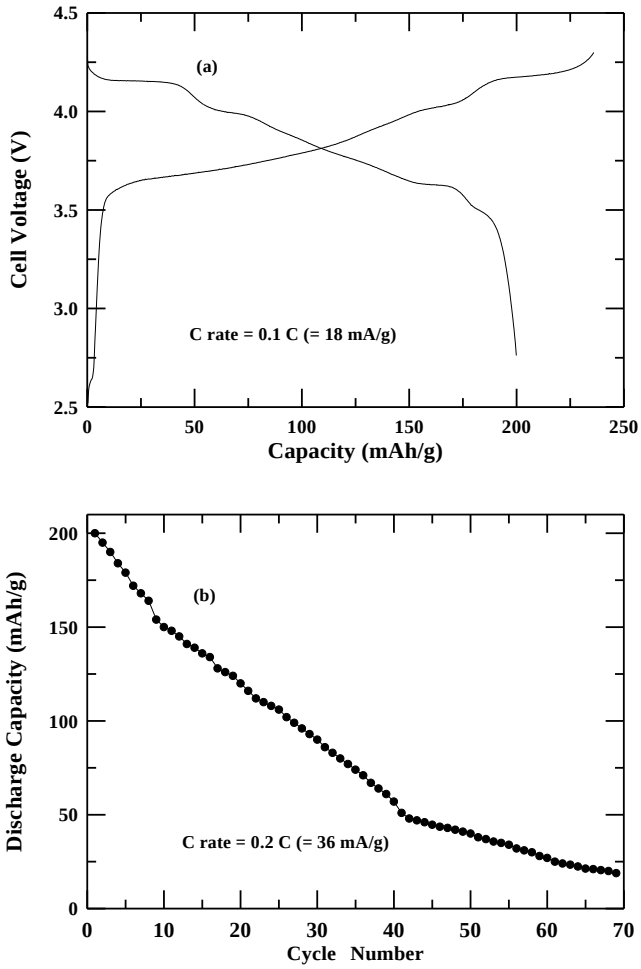

Figure 15. (a) Initial voltage profiles of $LiNiO_2$ between 4.3 and 2.75 V at a rate of 0.1 C (18 mA/g), and (b) cycle life of $LiNiO_2$ at a rate of 0.2 C (36 mA/g).

Several reversible structural transitions occur upon Li deintercalation [31,34,38], which are different from those occurring in $Li_{1-x}CoO_2$ (Fig. 16). CVs up to 4.4 V show $H1 \leftrightarrow M \leftrightarrow H2 \leftrightarrow H3$ transformations and high initial charge and discharge capacities. However, a large capacity fade on long-term cycling was also observed (Fig. 15(b)). This behavior can be attributed to the migration of Ni cations from the layers to the interlayer space, thereby altering the subsequent electrochemical behavior [12,39]. In addition, since metal oxides with a low ductility undergo mechanically-induced microcracks resulting from lattice strains, the reversibility of Li intercalation sharply deteriorates.

Microcrack formation in each $LiNiO_2$ particle is induced by anisotropic lattice changes along the *a* and *c* axis in the initial hexagonal phase (Fig. 17) [38,40]. A similar behavior is observed in $LiCoO_2$.

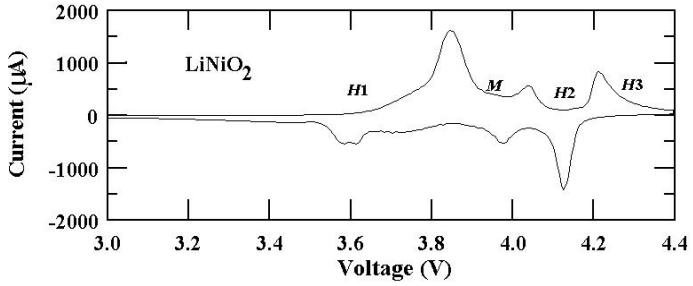

Figure 16. Cyclic voltammograms of $LiNiO_2$. The scan rate was 0.02 mV/sec.

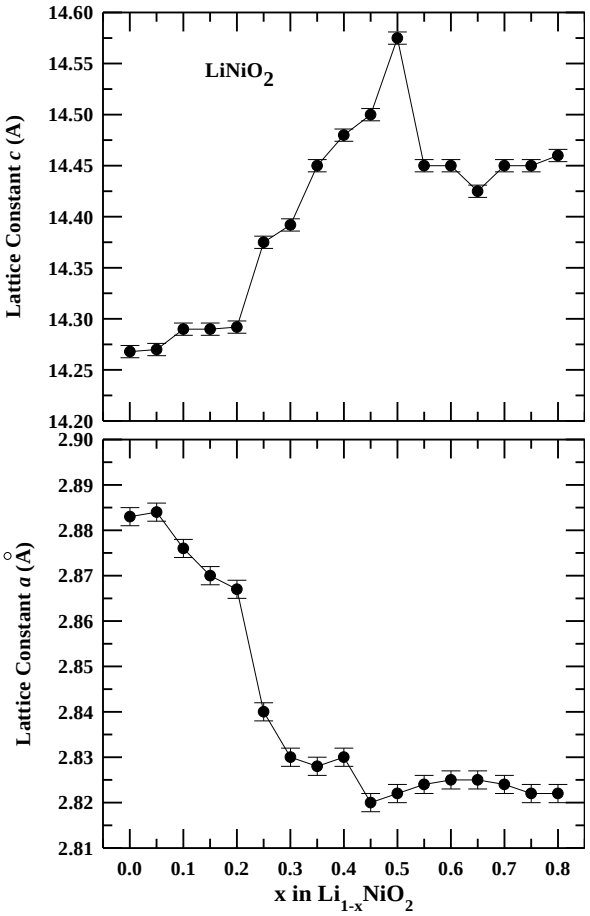

Figure 17. Evolution of the lattice constants *a* and *c* as a function of x in $Li_{1-x}NiO_2$.

3. METAL-OXIDE COATING ON $LiCoO_2$ POWDERS

3.1. Introduction

The electrochemical cycling of $LiCoO_2$ at a high cutoff voltage results in a significant deterioration of the stability of the cathode. As commented above, this capacity loss is related to non-uniform structural changes [1,13-19] and an increase in cobalt dissolution into the electrolyte [20]. To improve the electrochemical performance of $LiCoO_2$ above 4.2 V, an innovative approach was adopted. This involved coating the particles with some metal oxides to avoid the unwanted surface reaction and protect the bulk [5,16-19,41-47]. This method changes the surface properties of the cathode materials. Aurbach *et al.* [48] reported that the electrochemical behavior of Li_xMO_y (M = Ni, Mn) cathode materials is strongly dependent on their surface chemistry. Recent reports on surface modifications to cathode materials such $LiCoO_2$ and $LiNiO_2$ with Al_2O_3, ZrO_2, MgO, ZnO_2, Ga_2O_3, and SnO_2 have shown that surface coating is an effective way to stabilize the structure of the materials and improve their electrochemical performance.

3.2. Preparation of Metal-Oxide Coated $LiCoO_2$ Powders

A sol-gel coating of various metal oxides having a wide range of fracture toughness (ZrO_2, Al_2O_3, TiO_2, B_2O_3, and SiO_2) [49-51] is applied on the $LiCoO_2$ particle surfaces. Metal ethylhexanate-diisopropoxide ($M(OOC_8H_{15})(OC_3H_7)_2$) is dissolved in 2-propanol, followed by continuous stirring at RT. The $LiCoO_2$ powder (average particle size of ~10 μm) is then mixed with the coating solution such that the total concentration of metal in the coating solution corresponds to 5 wt. % of the $LiCoO_2$ powders used. The resulting solution is further aged at 50°C to allow the M-OR groups to react with the $LiCoO_2$ surface-OH groups, leading to strong bonds between the metal-oxide gel and the $LiCoO_2$ particle surface. After drying, each coated $LiCoO_2$ powder is fired at 400°C for some hours. Field-emission SEM confirms that the metal-oxide coating is continuous. X-ray diffraction of the as-prepared samples show a single-phase α-$NaFeO_2$ structure ($R\bar{3}m$), where the cobalt and lithium ions are located at the 3*a* and 3*b* octahedral sites, respectively, in a close-packed oxygen array. However, the XRD patterns of the coated samples

do not show any evidence of a crystalline metal oxide. Enhanced electrochemical results have been observed by a metal-oxide coating from Dahn's group [42]. However, they have shown that the coating layer contains nanocrystalline ZrO_2 (15-25 nm) on the surface of the $LiCoO_2$ powders through their XRD pattern and TEM image. This discrepancy may be due to the difference in the coating precursors. The coating solutions used by Dahn's group are a zirconium oxide polymeric precursor or an aqueous solution of $ZrO(NO_3)_2 \cdot xH_2O$.

3.3. Cycle-Life Performance of Metal-Oxide Coated $LiCoO_2$

To test the cycle-life performance of each cathode material, coin-type half cells ($Li/LiCoO_2$) are cycled at the 0.1 C rate (14 mA/g) for the first 2 cycles between 4.4 and 2.75 V. Cycling is then continued at the 0.5 C rate for up to 70 cycles. As shown in Fig. 18, the initial discharge capacities of the ZrO_2- and Al_2O_3-coated samples are similar to that of the uncoated one, and the cycle-life performance trend is consistent with the fracture toughness of the coated metal oxide ($ZrO_2 > Al_2O_3 > TiO_2 > B_2O_3 > SiO_2$). In addition, the ZrO_2-coated sample does not show any noticeable capacity fading over 70 cycles. In contrast, bare $LiCoO_2$ loses ~40% of its original capacity after only 30 cycles.

The lattice constant *c* as a function of x in the hexagonal $Li_{1-x}CoO_2$ from x = 0 to 0.7 during the first charge is shown in Fig. 19. Even though the lattice constant *a* shows a slight variation during charging in both the bare and coated $Li_{1-x}CoO_2$, the lattice-constant *c* shifts depend on the choice of the metal-oxide coating. The stability of the *c*-axis dimension correlates well with the fracture toughness of the coated oxides, and occurs in the order of $ZrO_2 > Al_2O_3 > TiO_2 > B_2O_3 > SiO_2$. This result confirms that suppressing the non-uniform strain during the delithiation produces a new-class of cathode materials, which are extremely tolerant to electrochemical cycling. Note that the lattice constant *c* of the ZrO_2-coated $LiCoO_2$ exhibits a negligible shift in the range $0 < x < 0.7$. In addition, a sol-gel coating of ZrO_2 can effectively inhibit cobalt dissolution from the $LiCoO_2$ cathodes. As shown in Fig. 20, cobalt dissolution of ZrO_2-coated $LiCoO_2$ (~140 ppm) is effectively suppressed, compared to that of an uncoated $LiCoO_2$ (~730 ppm), after a charge to 4.8 V and one-week storage at 25°C. Amatucci *et al.* reported that an

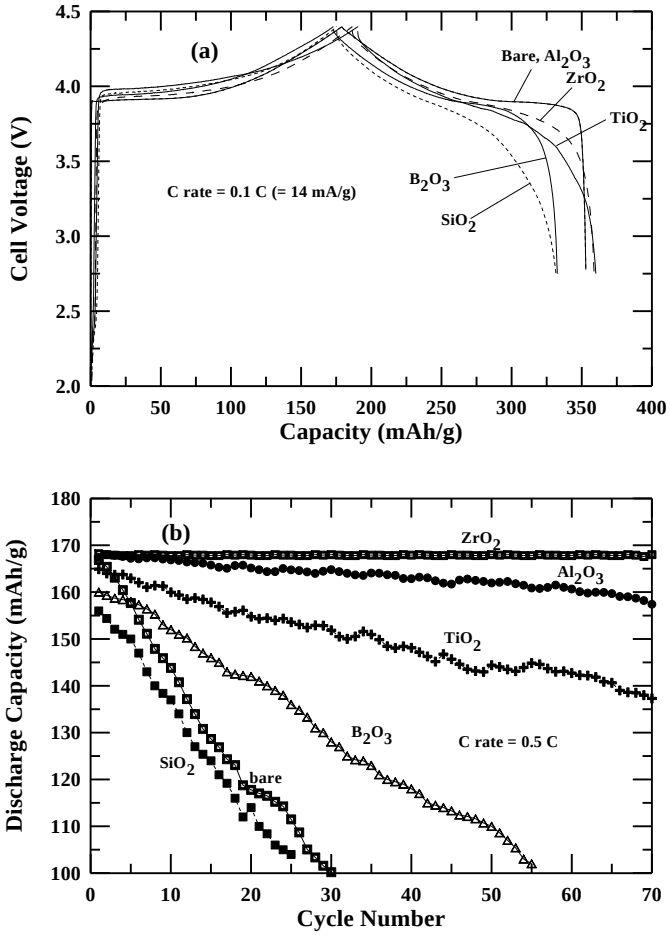

Figure 18. (a) Initial charge and discharge curves for various metal-oxide coated $LiCoO_2$, and comparison with uncoated $LiCoO_2$ (first cycle). (b) Cycle-life performances for ZrO_2-, Al_2O_3-, TiO_2-, B_2O_3-, SiO_2-coated, and uncoated $LiCoO_2$. The cells were cycled at a rate of 0.1 C for the first two cycles, followed by a 0.5 C rate between 4.4 and 2.75 V at 21°C.

increase in cobalt dissolution above 4.4 V is related to the lattice changes by the removal of the binding lithium [12]. Figure 21 depicts how enclosing the $LiCoO_2$ particles in a fracture-toughened metal-oxide coating layer can effectively suppress the non-uniform lattice-constant changes during Li deintercalation. It should be noted that, in thin film $LiCoO_2$ (both bare and metal-oxide coated), the lattice constants as a function of the cell voltage from OCV to 4.4 V show negligible *c*-axis expansion (details in §4.2.5). Dahn's group suggests that a ZrO_2 coating

on the powder has no effect on Li_xCoO_2 expansion during charging/discharging although the ZrO_2-coated $LiCoO_2$ powders exhibit an improved cycling behavior to 4.5 V compared to the uncoated samples [42]. This disagreement is probably due to the difference in the coating solution. Dahn's group assumes that a ZrO_2 coating may inhibit side reactions involving oxygen loss from the Li_xCoO_2 to the electrolyte and hence improve the cycling stability.

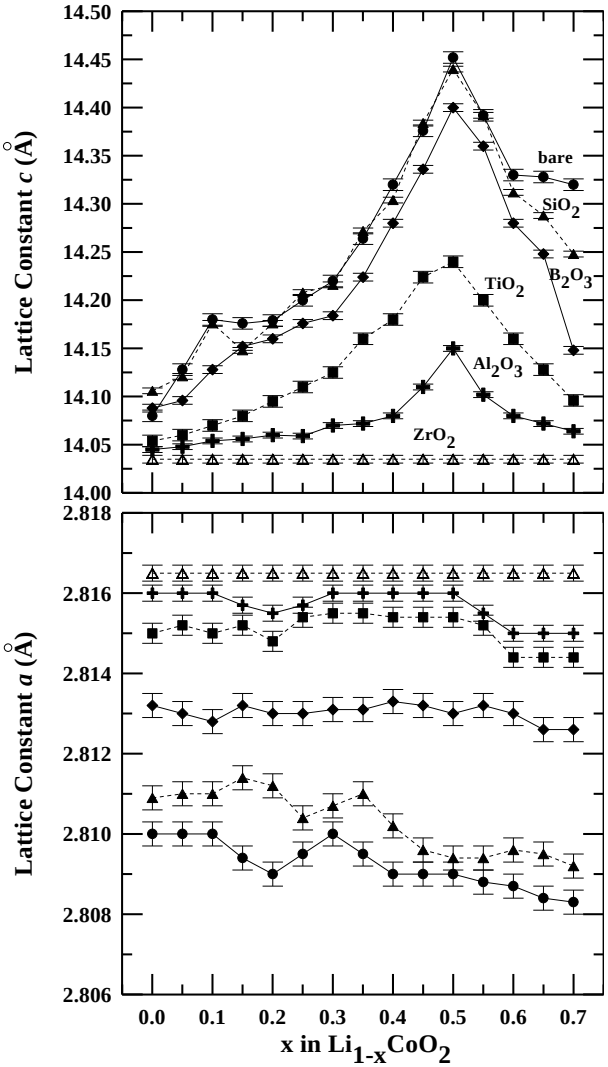

Figure 19. Lattice constants *a* and *c* in ZrO_2-, Al_2O_3-, TiO_2-, B_2O_3-, SiO_2-coated, and bare $LiCoO_2$ as a function of x in $Li_{1-x}CoO_2$ during the first charge. The precursor is metal ethylhexanate-diisopropoxide ($M(OOC_8H_{15})(OC_3H_7)_2$) dissolved in 2-propanol.

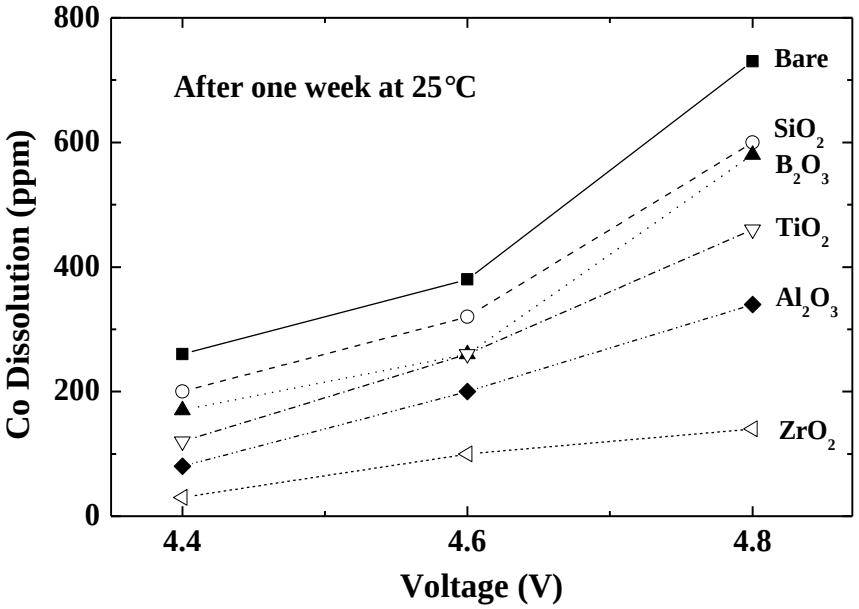

Figure 20. The amount of cobalt dissolution in the electrolyte, from various metal-oxide coated and uncoated $LiCoO_2$, after an initial charge and being immersed for one week at 25°C.

Figure 21. Schematic illustration of the suppression of lattice expansion from hexagonal to monoclinic phase by a nanoscale metal-oxide coating.

4. THIN-FILM $LiCoO_2$ CATHODE

4.1. Introduction

Thin film microbatteries [52-54] have potential applications in microelectronics. In particular, the fabrication of lithiated intercalation oxides in a thin-film form is of great interest because of their possible use as a positive electrode in all-solid-state lithium rechargeable microbatteries. This is due to the need to miniaturize various electronic devices, such as monolithic hybridization with CMOS-RAM, back-up power systems for computer chips, small sensors, and hazard cards [55-58]. Thin-film cathodes have also received a great deal of attention as they allow to study the intrinsic electrochemical properties of lithiated transition-metal oxides. Indeed, composite powders with polymer binders and carbon blacks may not represent the characteristic electrochemical properties of these oxides [57-67].

4.2. Electrochemical Properties of Al_2O_3-Coated $LiCoO_2$ Thin Films

4.2.1. Cycle-Life Performance of Al_2O_3-Coated $LiCoO_2$ Thin Films

To test the cycle-life performance of bare and 30 nm-thick Al_2O_3-coated $LiCoO_2$ thin films on a Pt/Si substrate, half cells are cycled in the voltage range 2.75 - 4.4 V at 0.2 mA/cm^2, as shown in Fig. 22. A 30 nm-thick Al_2O_3 coating significantly improves the electrochemical stability of the $LiCoO_2$ thin-film cathodes. The charge and discharge capacities of bare $LiCoO_2$ get deteriorated to only ~3% and ~25% of the original capacity after 100 cycles (Fig. 22(a)), while Al_2O_3-coated $LiCoO_2$ retains ~64% and ~75% of the initial capacity at a current rate of 0.2 mA/cm^2 (Fig. 22(b)). The charge capacities of the bare $LiCoO_2$ films (Li deintercalation) exhibit faster deterioration than the discharge capacities (Li intercalation). The effect of an Al_2O_3 coating on the cycle-life performance is more pronounced at a higher-current rate (Fig. 23). The insets in Fig. 22 show the same cycle-life performance, including the extra capacity from the constant voltage mode (at 4.4 V and 2.75 V).

In the bare samples, most of the charge capacity after ~40 cycles comes from the constant voltage charge of 4.4 V, indicating that the Li deintercalation kinetics are slower than the Li intercalation kinetics. On

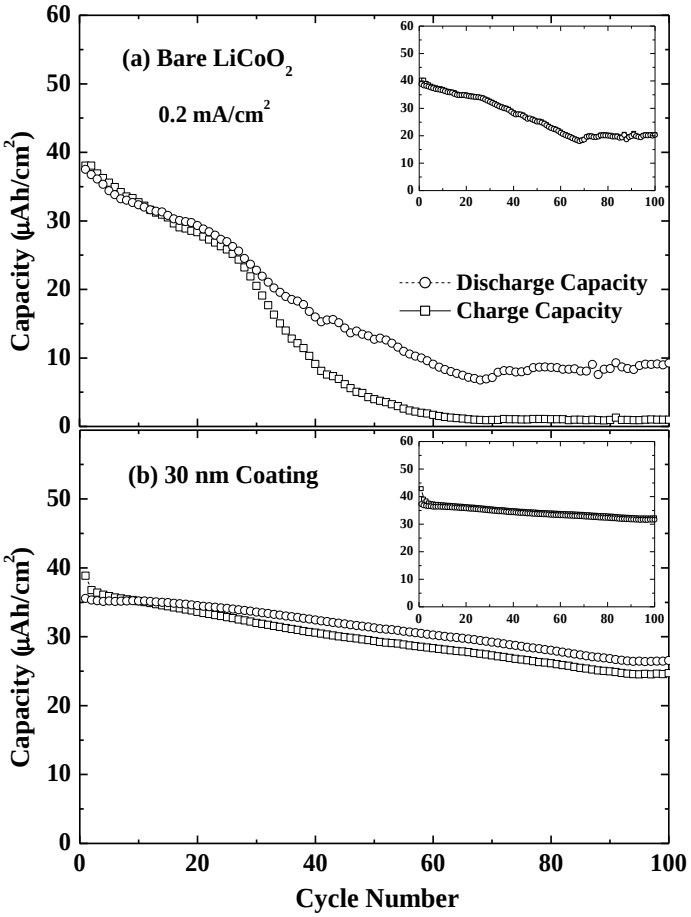

Figure 22. Cycle-life performance (charge and discharge capacities vs. cycle number) of (a) bare, and (b) 30 nm-thick Al_2O_3-coated $LiCoO_2$ thin films between 4.4 and 2.75 V at 0.2 mA/cm^2 (≈ 6 C). The inset shows the same cycle-life performance, including the extra capacity from the constant-voltage mode.

the other hand, the Al_2O_3-coated samples exhibit similar charge and discharge capacities, and the curve in the inset of Fig. 22(b) has an almost constant slope. This means that Li intercalation and deintercalation in the coated films become more symmetrical. The Al_2O_3 coating on the surface modifies the properties of the cathode surface exposed to the electrolyte and changes the Li-diffusion kinetics. The voltage profiles of the bare and 30 nm-thick Al_2O_3-coated $LiCoO_2$ thin films are shown in Fig. 24. The profiles of the bare $LiCoO_2$ thin films become steeper with increasing the cycling number up to 80 cycles at 0.2 mA/cm^2. In contrast, the change in

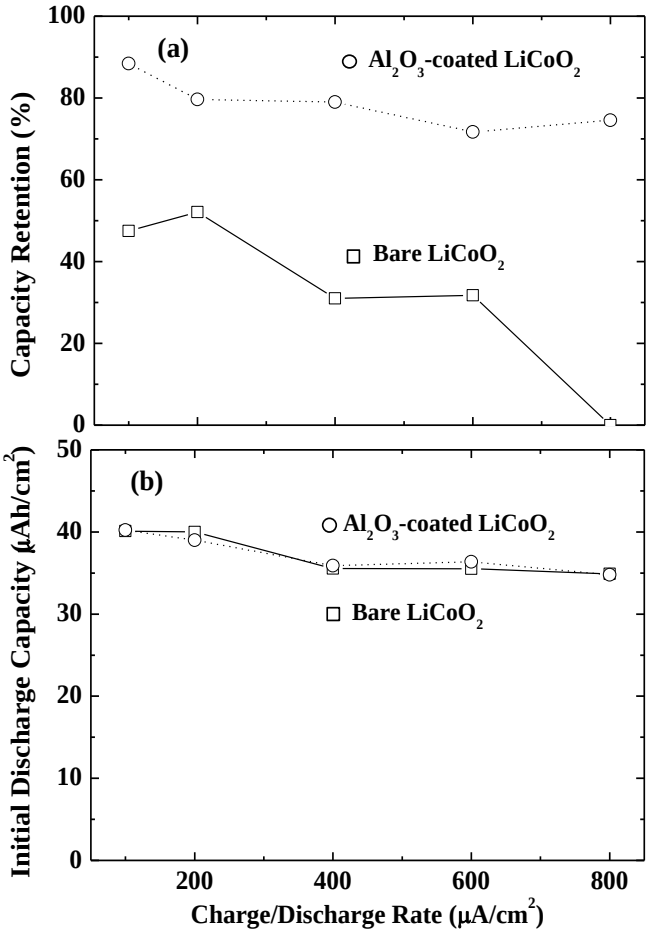

Figure 23. (a) Capacity retention vs. current rate after 100 cycles, and (b) initial discharge capacity vs. current rate of uncoated and Al_2O_3-coated $LiCoO_2$ thin films.

the voltage profiles of the Al_2O_3-coated $LiCoO_2$ thin films during 80 cycles is more gradual. However, compared with the cycling profiles of bare $LiCoO_2$ thin films, the slight increase in cell potential is observed in the initial cycle of Al_2O_3-coated cathodes. This is attributed to the insulation of aluminum-oxide layer on the surface to the Li ions. From the 2nd cycle on, the polarization in the charge and discharge processes of coated sample is not significant, which is because Li-Al-O coating layer on the $LiCoO_2$ acts as a solid electrolyte (details in §4.2.2).

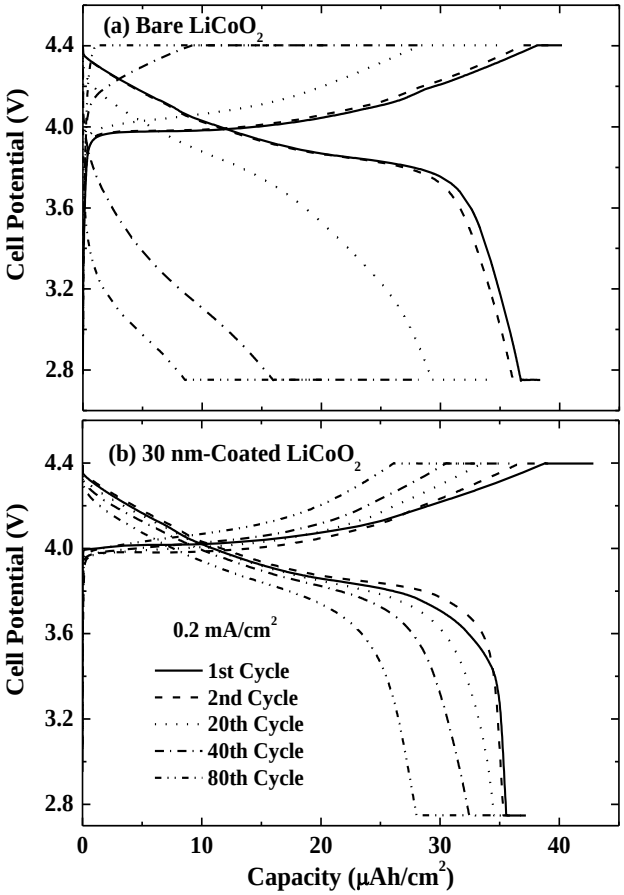

Figure 24. Voltage profiles of (a) uncoated, and (b) 30 nm-thick Al_2O_3-coated $LiCoO_2$ films between 4.4 and 2.75 V at a rate of 0.2 mA/cm^2. At each charge/discharge cutoff step, the cell voltage was potentiostated until the current decreased to 0.02 mA/cm^2.

4.2.2. Al_2O_3 Coating Layer Acting as a Solid Electrolyte

The Al_2O_3-coating thicknesses were varied from 10 nm to 300 nm to examine the possible questions of electronic insulation and Li migration through the Al_2O_3 layer. Figure 25(a) shows that the initial discharge capacities are almost independent of the coating thickness (0-300 nm range). In addition, the variation in the Al_2O_3 thickness ranging from 10 nm to 300 nm does not affect the capacity retention: ~70% and ~60%

retention, respectively, at 0.2 and 0.4 mA/cm^2, while the capacity retention of the uncoated $LiCoO_2$ thin film is only ~25% after 100 cycles, as shown in Fig. 25(b). This is possibly because the Al_2O_3 coating layer acts as a solid electrolyte with a low electronic conductivity and a reasonably high Li-ion conductivity. For example, the Li-ion conductivity of a $0.7Li_2O$-$0.3Al_2O_3$ solid electrolyte is ~10^{-7} S/cm at room temperature [68].

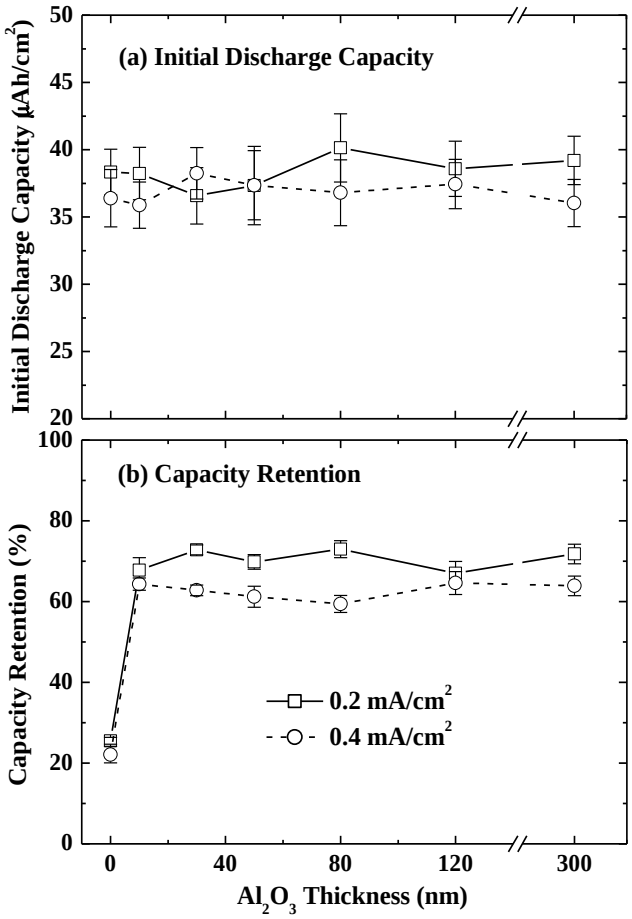

Figure 25. The effect of the Al_2O_3-coating thickness on (a) capacity retention after 100 cycles, and (b) initial discharge capacity, all excluding the extra capacity from the constant-voltage mode. The cells were cycled between 4.4 and 2.75 V at 0.2 and 0.4 mA/cm^2.

4.2.3. Suppression of Cobalt Dissolution by Al_2O_3 Coating

To clarify the reason why the Al_2O_3-coated $LiCoO_2$ thin films showed better electrochemical performance than the bare ones, inductively coupled plasma-mass spectroscopy (ICP-MS) analysis was carried out after floating at 4.2 V, 4.4 V, 4.5 V, 4.6 V, and 4.7 V, respectively, for 12 days. As shown in Fig. 26, the amount of cobalt dissolution from the uncoated $LiCoO_2$ films significantly increases with increasing the charge-cutoff voltages, while an increase in cobalt dissolution from the Al_2O_3-coated ones is not significant. An increase in the fraction of Co^{4+} in $Li_{1-x}CoO_2$ augments the reactivity with the electrolytes and acidic HF in the electrolyte. An Al_2O_3 coating can effectively inhibit cobalt dissolution even at 4.7 V (~100 ppm), which is much smaller than cobalt dissolution (~1000 ppm) from the uncoated $LiCoO_2$ films.

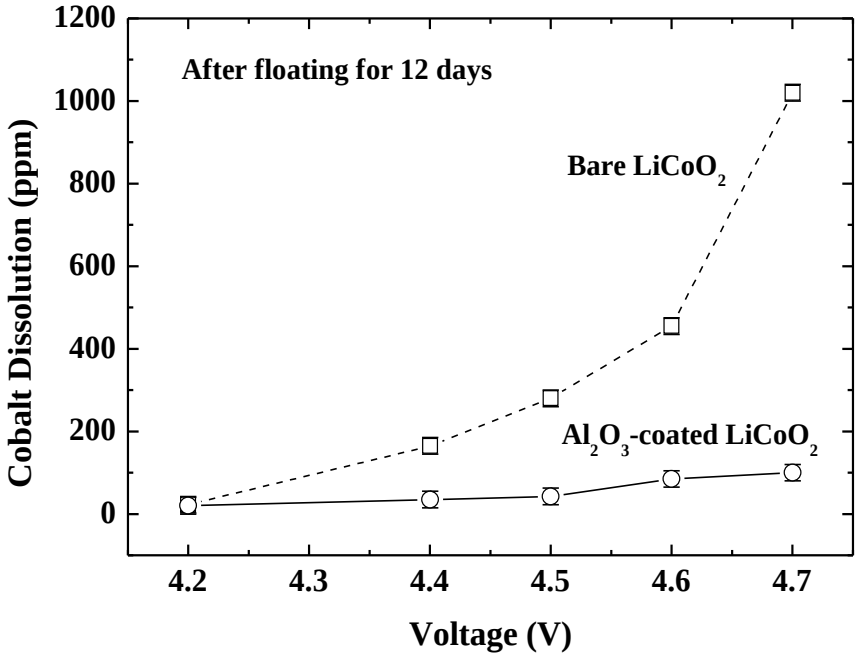

Figure 26. The amount of cobalt dissolution in the electrolyte (with 1 ㎖), from bare and Al_2O_3-coated $LiCoO_2$, after an initial charge and being immersed for 12 days at 25°C.

4.2.4. CV Measurement of Al_2O_3-Coated $LiCoO_2$ Thin Films

Figure 27 shows the cyclic voltammograms (CVs) of the bare and 30 nm-thick Al_2O_3-coated $LiCoO_2$ thin films at a scan rate of 0.1 mV/sec, which were carried out during the 1st cycle, and after the 40th and 80th charging/discharging cycles. The CVs of the Al_2O_3-coated $LiCoO_2$ thin films during the 1st cycle clearly show three sets of well-defined current peaks, i.e. the first set (~3.96 and ~3.87 V at *a* and *a*′), the second set (~4.07 and ~4.05 V at *b* and *b*′), and the third set (~4.19 and ~4.16 V at *c* and *c*′). The first set is due to the first-order phase transition between the two hexagonal phases, and the second and third sets are caused by the phase transition between the hexagonal and monoclinic phases [8,9]. These values are in good agreement with those obtained from the uncoated $LiCoO_2$ films and powders. However, these thin-film results are different from the CVs in the Al_2O_3-coated $LiCoO_2$ powders [16,18], and the reasons for this disparity need to be identified. The cathodic peak (~3.87 V at *a*′) of the Al_2O_3-coated film during the 1st cycle is narrower than that of the bare one, although the anodic peaks (~3.96 V at *a*) are similar. In addition, in the bare $LiCoO_2$ thin films, the widths of both the cathodic and anodic peaks are remarkably broadened, and the peak positions become more separated as the number of cycle increases to 80, while the widths of the cathodic and anodic peaks of the Al_2O_3-coated samples are relatively sharp. This indicates that the Al_2O_3-coated $LiCoO_2$ thin films are more reversible than the bare ones, which is probably related to the suppression of cobalt dissolution from the cathode (Fig. 26).

4.2.5. Changes in the Lattice Constants *c* as a Function of the Cell Potential

Figure 28 shows the changes in the lattice constants *c* as a function of the cell potential during the first charge in the $Li_{1-x}CoO_2$ thin films and powders [16-18]. Both the bare and Al_2O_3-coated $LiCoO_2$ thin films exhibit negligible *c*-axis expansion even with a strong (003) texture [67]. This is in contrast to the $LiCoO_2$ powders, which exhibit ~2.6% *c*-axis expansion at ~4.17 V. Further studies are necessary to identify the mechanisms that $LiCoO_2$ thin films have a limited *c*-axis expansion.

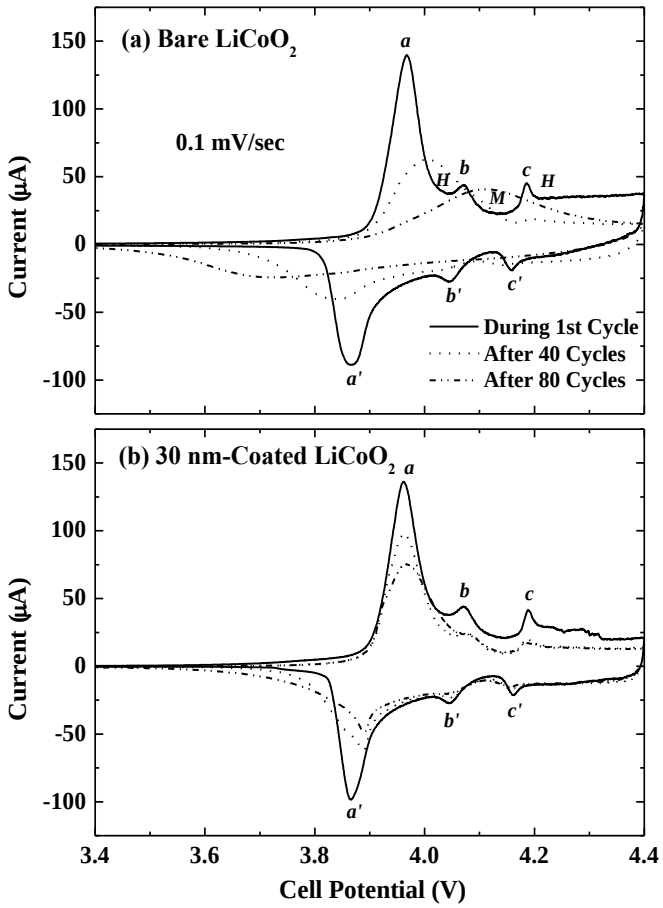

Figure 27. Cyclic voltammograms of (a) bare, and (b) 30 nm-thick Al_2O_3-coated $LiCoO_2$ thin films, during the 1st cycle, and after the 40th and 80th cycles. The sweep rate was 0.1 mV/sec between 3.0 and 4.4 V. The symbols *H* and *M* denote the hexagonal and monoclinic phases, respectively.

4.2.6. Li Diffusivities of Al_2O_3-Coated $LiCoO_2$ Thin Films

Figures 29 and 30 show the apparent Li diffusivities as a function of the cell potential of the $Li_{1-x}CoO_2$ cathodes during Li deintercalation (charging) and intercalation (discharging), respectively. The Li diffusivities of Al_2O_3-coated $LiCoO_2$ are slightly lower than those of bare one during the 1st Li deintercalation, as shown in Fig. 29. The Li

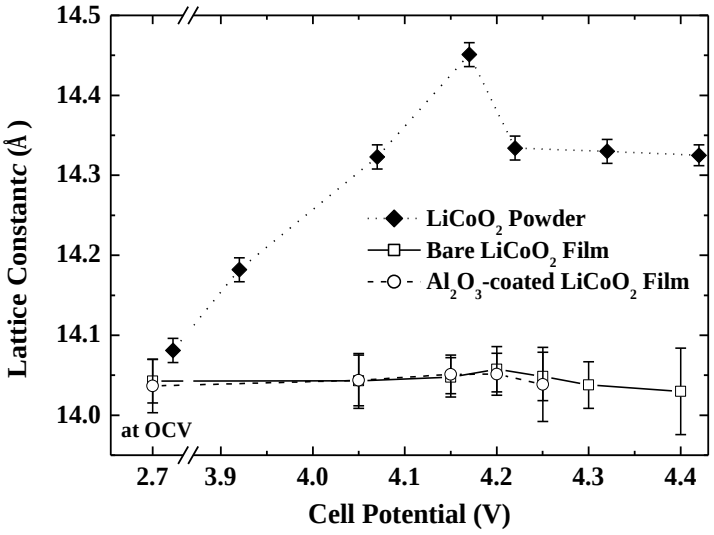

Figure 28. Changes in the lattice constants *c* as a function of the cell potential for bare and Al_2O_3-coated $LiCoO_2$ thin films during the first charge, with a comparison with powder samples. For thin films, each cell was charged at a 0.1 mA/cm^2 rate to the predetermined voltages, then potentiostated until the current density decreased to 1 $\mu A/cm^2$.

diffusivities in the bare $LiCoO_2$ thin films during Li deintercalation (Fig. 29) are in good agreement with the previous results obtained using either thin-film $Li_{1-x}CoO_2$ cathodes [57,58,62,69] or powder electrodes [70-72]. Note that the plots of the Li diffusivity vs. the cell potential show a maxima at ~4.13 V, corresponding to the monoclinic phase. In addition, two minima are observed at the cell potential corresponding to the phase transition between the hexagonal and monoclinic phase, which is similar to the previous reports by Jang *et al.* [60].

As the cycling number increases, the Li diffusivity decreases owing to the degradation of the thin-film $LiCoO_2$ cathodes. As shown in Fig. 29, during Li deintercalation (charging), the Li diffusivities of the bare $LiCoO_2$ thin films (in the range of approximately 4.15 and 4.3 V) decrease to ~5×10^{-12} cm^2/sec after 80 cycles, compared to ~2×10^{-11} cm^2/sec in the coated films. During Li intercalation (discharging), the Li diffusivities in

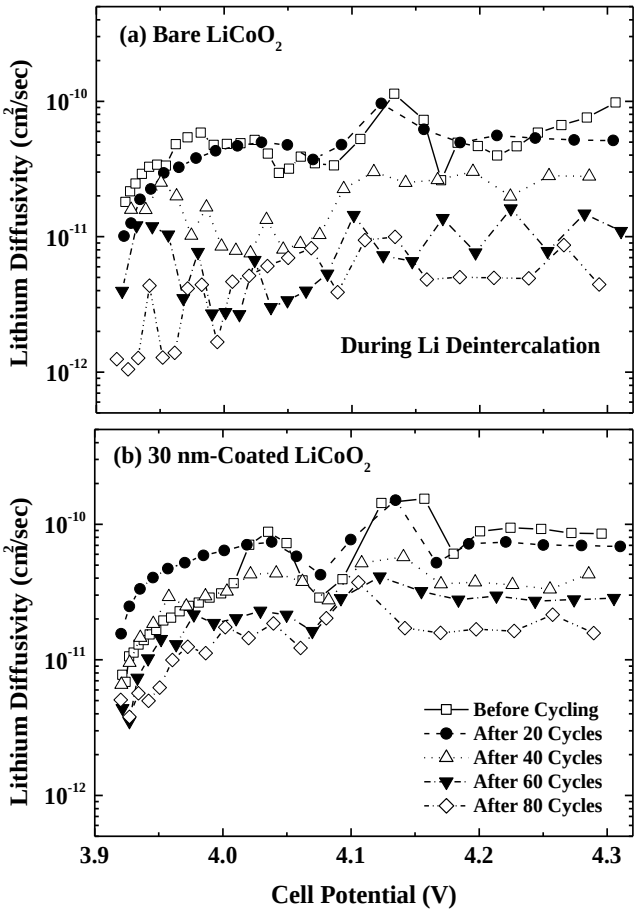

Figure 29. Lithium diffusivities as a function of the cell potential for (a) bare, and (b) 30 nm-thick Al_2O_3-coated $LiCoO_2$ thin films, determined by GITT during Li deintercalation (charging).

bare samples are ~1×10^{-11} cm^2/sec after 80 cycles, while the deterioration in the Li diffusivities in the coated ones remains at ~3×10^{-11} cm^2/sec (Fig. 30). These results suggest that an Al_2O_3 coating on the $LiCoO_2$ thin films can tolerate the electrochemical cycling with a high cutoff voltage of 4.4 V, which are attributed to the suppression of cobalt dissolution by Al_2O_3 coating.

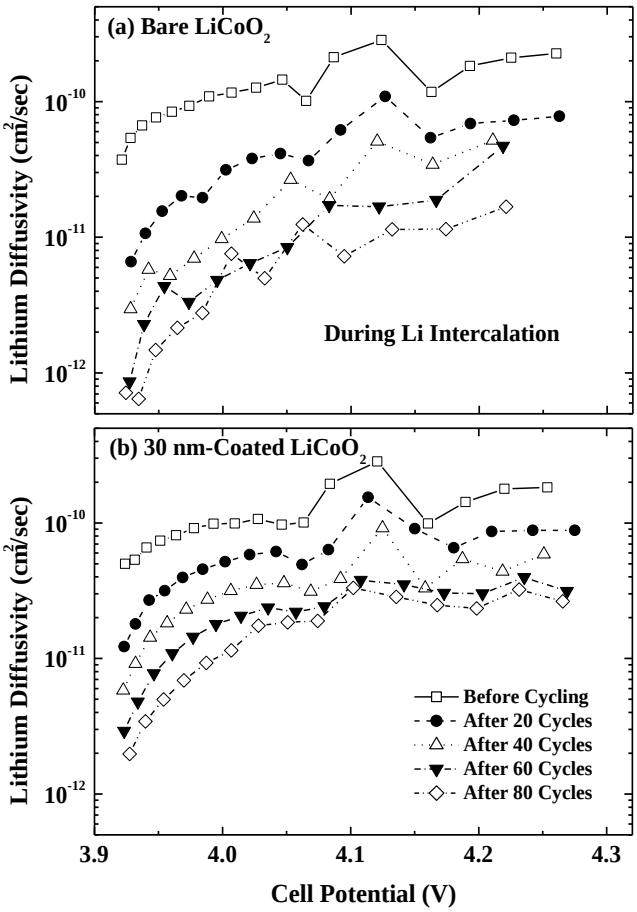

Figure 30. Lithium diffusivities as a function of the cell potential for (a) bare, and (b) 30 nm-thick Al_2O_3-coated $LiCoO_2$ thin films, as determined by GITT during Li intercalation (discharging).

4.3. Future Work

Further studies to detail the effect of a metal-oxide coating on the surface reactions, such as the microstructural changes in $Li_{1-x}CoO_2$, the composition profile of the Li-Al-O coating layer, and the electric-potential distribution near the interface between the $LiCoO_2$ cathode and the Li-Al-O coating layer, are currently underway. Also, the coating effects of various oxides need to be identified.

Acknowledgement

We are grateful to Joon-Gon Lee, Hyemin Kim, Tae-Joon Kim, and Byoungsoo Kim for their help to improve the clarity of this manuscript.

REFERENCES

1. H. Wang, Y.-I. Jang, B. Huang, D. R. Sadoway, and Y.-M. Chiang, *J. Electrochem. Soc.* **146**, 473 (1999).
2. H. Tukamoto and A. R. West, *J. Electrochem. Soc.* **144**, 3164 (1997).
3. Y.-I. Jang, B. Huang, H. Wang, D. R. Sadoway, G. Ceder, Y.-M. Chiang, H. Liu, and H. Tamura, *J. Electrochem. Soc.* **146**, 862 (1999).
4. W.-S. Yoon, K.-K. Lee, and K.-B. Kim, *J. Electrochem. Soc.* **147**, 2023 (2000).
5. M. Mladenov, R. Stoyanova, E. Zhecheva, and S. Vassilev, *Electrochem. Commun.* **3**, 410 (2001).
6. K. Mizushima, P. C. Jones, P. J. Wiseman, and J. B. Goodenough, *Mater. Res. Bull.* **15**, 783 (1980).
7. H. J. Orman and P. J. Wiseman, *Acta Crystallogr., Sect. C: Cryst. Struc. Commun.* **40**, 12 (1984).
8. J. N. Reimer and J. R. Dahn, *J. Electrochem. Soc.* **139**, 2091 (1992).
9. T. Ohzuku and A. Ueda, *J. Electrochem. Soc.* **141**, 2972 (1994).
10. J. van Elp, J. L. Wieland, H. Eskes, P. Kuiper, G. A. Sawatzky, F. M. F. de Groot, and T. S. Turner, *Phys. Rev. B* **44**, 6090 (1991).
11. J. Molenda, A. Stoklosa, and T. Bak, *Solid State Ionics* **36**, 53 (1989).
12. G. G. Amatucci, J. M. Tarascon, and L. C. Klein, *J. Electrochem. Soc.* **143**, 1114 (1996).
13. H. Wang, Y.-I. Jang, B. Huang, D. R. Sadoway, and Y.-M. Chiang, *J. Power Sources* **81-82**, 594 (1999).
14. Y.-K. Sun, *J. Power Sources* **83**, 223 (1999).
15. Y.-M. Choi and S.-I. Pyun, *Solid State Ionics* **99**, 173 (1997).
16. J. Cho, Y. J. Kim, and B. Park, *Chem. Mater.* **12**, 3788 (2000).
17. J. Cho, Y. J. Kim, T.-J. Kim, and B. Park, *Angew. Chem. Int. Ed.* **40**, 3367 (2001).
18. J. Cho, Y. J. Kim, and B. Park, *J. Electrochem. Soc.* **148**, A1110 (2001).
19. J. Cho, C.-S. Kim, and S.-I. Yoo, *Electrochem. Solid-State Lett.* **3**, 362 (2000).
20. G. G. Amatucci, J. M. Tarascon, and L. C. Klein, *Solid State Ionics* **83**, 167 (1996).
21. K. Dokko, M. Mohamede, Y. Fujita, T. Itoh, M. Nishizawa, M. Umeda, and I. Uchida, *J. Electrochem. Soc.* **148**, A442 (2001).

22. G. Ceder, Y.-M. Chiang, D. R. Sadoway, M. K. Aydinol, Y.-I. Jang, and B. Huang, *Nature* **392**, 694 (1998).
23. S.-T. Myung, N. Kumagai, S. Komaba, and H.-T. Chung, *Solid State Ionics* **139**, 47 (2001).
24. K. Kubo, M. Fujiwara, S. Yamada, S. Arai, and M. Kanda, *J. Power Sources* **68**, 553 (1997).
25. C.-C. Chang, J. Y. Kim, and P. N. Kumta, *J. Electrochem. Soc.* **149**, A331 (2002).
26. J. Cho, G. Kim, and H. S. Lim, *J. Electrochem. Soc.* **146**, 3571 (1999).
27. Z. Lu, D. D. MacNeil, and J. R. Dahn, *Electrochem. Solid-State Lett.* **4**, A200 (2001).
28. M. M. Thackeray, *J. Electrochem. Soc.* **142**, 2558 (1995).
29. P. G. Bruce, *Chem. Commun.*, 1817 (1997).
30. P. Koksbang, J. Barker, H. Shi, and M. Y. Sakdi, *Solid State Ionics* **84**, 1 (1996).
31. H. Arai, S. Okada, H. Ohtsuka, M. Ichimura, and J. Yamaki, *Solid State Ionics* **80**, 261 (1995).
32. T. Ohzuku, A. Ueda, and M. Nagayama, *J. Electrochem. Soc.* **140**, 1862 (1993).
33. A. Rougier, P. Gravereau, and C. Delmas, *J. Electrochem. Soc.* **143**, 1168 (1996).
34. J. Barker, R. Koksbang, and M. Y. Saidi, *Solid State Ionics* **89**, 25 (1996).
35. R. V. Moshtev, P. Zlatilova, V. Manev, and A. Sato, *J. Power Sources* **54**, 329 (1995).
36. H. Arai, S. Okada, Y. Sakurai, and J. I. Yamaki, *Solid State Ionics* **95**, 275 (1997).
37. J. P. Peres, PhD thesis, Univ. of Bordeaux I, France, (1996).
38. W. Li, J. N. Reimer, and J. R. Dahn, *Solid State Ionics* **67**, 123 (1993).
39. T. Ohzuku, A. Ueda, and M. Kouguchi, *J. Electrochem. Soc.* **142**, 4033 (1995).
40. J. Cho, H. Jung, Y. Park, G. Kim, and H. Lim, *J. Electrochem. Soc.* **147**, 10 (2000).
41. Z. Wang, C. Wu, L. Liu, F. Wu, L. Chen, and X. Huang, *J. Electrochem. Soc.* **149**, A466 (2000).
42. Z. Chen and J. R. Dahn, *Electrochem. Solid-State Lett.* **5**, A213 (2002).
43. Z. Wang, L. Liu, L. Chen, and X. Huang, *Solid State Ionics* **148**, 335 (2002).
44. J. Cho, T.-J. Kim, Y. J. Kim, and B. Park, *Electrochem. Solid-State Lett.* **4**, A159 (2001).
45. D. Rahner, W. Plieth, and M. Kloss, "Modified electrode material and its use," U.S. Patent No. 6348259, March 30, 1999.
46. T. Miyasaka, "Non-aqueous lithium ion secondary battery," U.S. Patent No. 6037095, March 30, 1998.
47. H.-J. Kweon, G.-B. Kim, and D.-G. Park, "Positive active material for rechargeable lithium battery and method of preparing same," U.S. Patent No. 6183911, October 29, 1999.
48. D. Aurbach, K. Gamosky, B. Markovsky, G. Salitra, Y. Gofer, U. Heider, R. Oesten, and M. Schmidt, *J. Electrochem. Soc.* **147**, 1322 (2000).
49. W. D. Jr. Callister, *Materials Science and Engineering: An Introduction*, John Wiley & Sons: New York, 4th ed., Appendix C, p. 787 (1997).

50. M. C. Fredel and A. R. Boccaccini, *J. Mater. Sci.* **31**, 4375 (1996).
51. J. Sehgal and S. Ito, *J. Non-Cryst. Solids* **253**, 126 (1999).
52. P. Birke, W. F. Chu, and W. Weppner, *Solid State Ionics* **93**, 1 (1997).
53. J. B. Bates, G. R. Gruzalski, N. J. Dudney, C. F. Luck, and X. Yu, *Solid State Ionics* **70-71**, 619 (1994).
54. C. Julien and G.-A. Nazri, *Solid State Batteries: Materials Design and Optimization*, Kluwer Academic, Boston, 1994.
55. C. Wolverton and A. Zunger, *J. Electrochem. Soc.* **145**, 2424 (1998).
56. D. G. Fauteux, A. Massucco, J. Shi, and C. Lampe-Onnerud, *J. Appl. Electrochem.* **27**, 543 (1997).
57. B. Wang, J. B. Bates, F. X. Hart, B. C. Sales, R. A. Zuhr, and J. D. Robertson, *J. Electrochem. Soc.* **143**, 3203 (1996).
58. J. B. Bates, N. J. Dudney, B. J. Neudecker, F. X. Hart, H. P. Jun, and S. A. Hackney, *J. Electrochem. Soc.* **147**, 59 (2000).
59. M. Antaya, J. R. Dahn, J. S. Preston, E. Rossen, and J. N. Reimers, *J. Electrochem. Soc.* **140**, 575 (1993).
60. Y.-I. Jang, B. J. Neudecker, and N. J. Dudney, *Electrochem. Solid-State Lett.* **4**, A74 (2001).
61. J.-K. Lee, S.-J. Lee, H.-K. Baik, H.-Y. Lee, S.-W. Jang, and S.-M. Lee, *Electrochem. Solid-State Lett.* **2**, 512 (1999).
62. K. A. Striebel, C. Z. Deng, S. J. Wen, and E. J. Cairns, *J. Electrochem. Soc.* **143**, 1821 (1996).
63. Y. Iriyama, M. Inaba, T. Abe, and Z. Ogumi, *J. Power Sources* **94**, 175 (2001).
64. J. D. Perkins, C. S. Bahn, J. M. McGraw, P. A. Parilla, and D. S. Ginley, *J. Electrochem. Soc.* **148**, A1302 (2001).
65. P. J. Bouwman, B. A. Boukamp, H. J. M. Bouwmeester, and P. H. L. Notten, *J. Electrochem. Soc.* **149**, A699 (2002).
66. J. D. Perkins, C. S. Bahn, P. A. Parilla, J. M. McGraw, M. L. Fu, M. Duncan, H. Yu, and D. S. Ginley, *J. Power Sources* **81-82**, 675 (1999).
67. Y. J. Kim, T.-J. Kim, J. W. Shin, B. Park, and J. Cho, *J. Electrochem. Soc.* **149**, 1337 (2002).
68. A. M. Glass and K. Nassau, *J. Appl. Phys.* **51**, 3756 (1980).
69. J. M. McGraw, C. S. Bahn, P. A. Parilla, J. D. Perkins, D. W. Readey, and D. S. Ginley, *Electrochim. Acta* **45**, 187 (1999).
70. J.-S. Hong and J. R. Selman, *J. Electrochem. Soc.* **147**, 3190 (2000).
71. M. D. Levi, K. Gamolsky, D. Aurbach, U. Heider, and R. Oesten, *J. Electroanal. Chem.* **477**, 32 (1999).
72. D. Aurbach, D. L. Levi, E. Levi, H. Teller, B. Markovsky, and G. Salitra, *J. Electrochem. Soc.* **145**, 3024 (1998).